https://doi.org/10.1038/s44454-026-00058-w

Revised direct radiative forcing of airborne microplastics suggests warming

Felix W. Goddard[1] ✉, Stefania Glukhova[2], Eric C. Le Ru[2], Nikolaos Evangeliou[3], Cameron McErlich[1], Catherine Hardacre[1], David Frame[1], Peter Kuma[4] & Laura E. Revell[1] ✉

Microplastics are a common airborne pollutant, capable of being transported over large distances and with potential to alter the radiative properties of the atmosphere in large enough quantities, with implications for global climate. Since the first estimates of microplastic radiative forcing were published in 2021, new constraints on many aspects of the spatial and temporal distribution of airborne plastics and their physical and optical properties have emerged. Using these updated findings concerning the size distribution of airborne microplastics, new spectral absorption data for coloured plastics, and a new microplastic emissions dataset, we investigate the sensitivity of the direct radiative effect of airborne microplastics. We find clear-sky effective radiative forcings ranging from −3.28 to +46.7 mW m^{-2} depending on assumptions concerning colour, size distribution, vertical profile and spatial distribution. Assuming likely real-world conditions—a mix of coloured microplastics, a power law size distribution and distributing microplastics non-uniformly through the troposphere based on a new emissions dataset—we calculate an updated estimate of +42.1 ± 4.62 mW m^{-2} for a global-average surface concentration of 3.99 microplastics m^{-3}. This revised radiative forcing is at least as large in forcing magnitude as the contributions of a number of other species routinely evaluated by the Intergovernmental Panel on Climate Change. Our findings suggest that microplastics are likely contributing to atmospheric warming and, given that plastic pollution is projected to increase, should be included in climate change projections.

In the past decade, microplastics (MPs, plastic particles <5 mm in diameter) have emerged as a ubiquitous pollutant in the atmosphere, both close to major MP emission sources and in remote locations alike[1,2]. MPs are emitted from a wide variety of primarily urban sources and, once in the atmosphere, undergo long-range transport[3–5]. The atmospheric burden of microplastics is projected to increase over time as the amount of plastic waste in the environment increases, given the absence of fast or effective removal pathways[6]. Alongside concerns over their human health effects[7], MPs have potential to act as a short-lived climate forcer similar to other atmospheric aerosols. Aerosols impact the Earth's climate by altering the passage of radiation through the atmosphere. This may occur by direct interactions between aerosol particles and radiation (the direct radiative effect) and by interactions between aerosols and clouds, which alter cloud albedo, extent and lifetime (the indirect radiative effect[8,9]). Recent work has demonstrated that MPs may impact cloud properties by acting as ice nucleating particles[10–13], and lower the surface albedo of snow and ice, accelerating melt rates[14,15].

Revell et al.[16] (hereafter R21) made the first estimate of the direct radiative effect of airborne MPs. They calculated a top-of-atmosphere (TOA) effective radiative forcing (ERF; see section 'Modelling of radiative effects') of +0.044 ± 0.399 mW m^{-2} for non-pigmented MPs assuming a gamma distribution of particle sizes, a uniform surface concentration of 1 MP m^{-3} and a vertical distribution up to 10 km altitude. Fibres were shown to have a larger ERF than fragments due to their size and shape. When confined to the lowest 2 km of the atmosphere, the microplastic ERF was −0.746 ± 0.553 mW m^{-2}. The assumptions used by R21 were a necessity due to the scarcity of data available at the time, but are significant simplifications that do not represent reality, evidenced by more recent studies. Yang et al.[17] and Pang et al.[18] present estimates of the MP direct radiative effect using more realistic (i.e. spatially varying) surface

[1]School of Physical and Chemical Sciences, University of Canterbury, Christchurch, New Zealand. [2]The MacDiarmid Institute for Advanced Materials and Nanotechnology, School of Chemical and Physical Sciences, Victoria University of Wellington, Wellington, New Zealand. [3]Department for Atmospheric & Climate Research (ATMOS), Stiftelsen NILU (formerly NILU - Norwegian Institute for Air Research), Kjeller, Norway. [4]Rossby Centre, Swedish Meteorological and Hydrological Institute, Norrköping, Sweden. ✉e-mail: felix.goddard@pg.canterbury.ac.nz; laura.revell@canterbury.ac.nz

Table 1 | Effective radiative forcing (ERF) derived from HadGEM3-GA7.1 simulations (defined in Table 2) and instantaneous radiative forcing (IRF) derived from analogous simulations with the SOCRATES radiative transfer model (see section 'Modelling of radiative effects')

	Simulation name	ERF (mW m^{-2})			IRF (mW m^{-2})			Total plastic burden (Tg)[b]
		SW	LW	Net	SW	LW	Net	
1	Previous estimate	−3.72 ± 0.40	+1.18 ± 0.57	−2.55 ± 0.73	−4.77	+1.79	−2.97	0.92
2	Mixed-colour	−0.45 ± 0.10	+1.06 ± 0.16	+0.61 ± 0.15	−1.13	+1.77	+0.64	0.92
3	TBWP [a]	+3.41 ± 0.77	+0.36 ± 1.19	+3.77 ± 1.13	+4.47	+1.25	+5.72[c]	0.92
4	Power law size distribution	−4.67 ± 0.62	+3.01 ± 0.59	−1.66 ± 0.65	−6.28	+3.32	−2.96[c]	1.00
5	Whole troposphere	−18.1 ± 0.19	+27.0 ± 0.27	+8.88 ± 0.27	−25.6	+28.4	+2.76[c]	4.28
6	Horizontally non-uniform	−2.70 ± 0.27	+1.19 ± 0.27	−1.51 ± 0.41	−3.63	+1.97	−1.66	0.91
7	Updated estimate	−3.47 ± 3.38	+45.5 ± 4.51	+42.1 ± 4.62	−0.52	+47.11	+46.6	4.69

Uncertainties for ERFs are the 5 to 95% confidence interval of the distribution of forcing values over the 20 simulation years, assumed to follow a *t*-distribution. Radiative forcings are scaled to a global-average surface concentration of 3.99 MP m^{-3} between 50 and 100 µm diameter, following Leusch et al.[22].

[a]Simulation 'TBWP' is named for tire- and brake-wear particles (TBWP; see section 'Microplastic refractive index').

[b]Total plastic burdens were calculated by integrating the MP number concentration over the globe, following the spatial distributions described in Spatio-temporal distribution of microplastics, and converting particle number to mass using the average particle volume of the assumed size distribution and an average plastic density of 1.1 g cm^{-3}.

[c]Net IRF does not fall within the 5–95% confidence interval of the corresponding net ERF.

Table 2 | Names and parameters of the seven simulations carried out

	Simulation name	Colour	Size distribution	Vertical distribution	Horizontal distribution[a]
1	Previous estimate	Colourless[b]	Gamma[c]	Confined to <2 km[e]	uniform, 1680 MP m^{-3}
2	Mixed-colour	Mixed-colour[b]	Gamma	Confined to <2 km	uniform, 7230 MP m^{-3}
2	TBWP	BC-containing[b]	Gamma	Confined to <2 km	uniform, 860 MP m^{-3}
4	Power law size distribution	Colourless	Power law[d]	Confined to <2 km	uniform, 5710 MP m^{-3}
5	Whole troposphere	Colourless	Gamma	Whole troposphere[f]	uniform, 2620 MP m^{-3}
6	Horizontally non-uniform	Colourless	Gamma	Confined to <2 km	non-uniform, 3070 MP m^{-3}
7	Updated estimate	Mixed-colour	Power law	Whole troposphere	non-uniform, 650 MP m^{-3}

All simulations were run for 21 years from 1 Sep 1988 with the first year discarded as spin-up. Global-average surface number concentrations prescribed in the horizontal distribution were increased in order to attain a clear signal-to-noise ratio in the ERF. Reported results have been scaled down to correspond to a global-average surface MP number concentration of 3.99 MP m^{-3} between 50 and 100 µm diameter (see section 'Microplastic morphotype and size distribution').

[a]Listed concentrations denote prescribed global-average surface MP number concentrations, corresponding to $[MP]_{simulated}$ in Eq. (5).

[b]Absorption and scattering cross-sections for colourless, mixed-colour and BC-containing plastics are shown in Fig. 3a, 3b and 3c, respectively.

[c]Gamma size distribution is given by Eq. (6).

[d]Power law size distribution is given by Eq. (7).

[e]'Confined to <2 km' vertical distribution is given by Eq. (10).

[f]'Whole troposphere' vertical distribution function is given by Eq. (11).

concentrations. Yang et al.[17] modelled an urban area in which high concentrations of MPs had been measured, finding a highly variable radiative forcing that was correlated with atmospheric and land surface conditions. Pang et al.[18] performed global atmospheric transport simulations and calculated a global net TOA radiative forcing of −6.34 µW m^{-2}, a net cooling in agreement with R21 but considerably smaller in magnitude. Liu et al.[19] used measurements of coloured plastics to show that pigmentation leads to increased absorption of solar radiation, and a shortwave radiative forcing of +6 mW m^{-2} for microplastics following the same size distribution used by R21. However, they did not model longwave effects.

Here we provide an exploration of the parameter space and an updated estimate of the direct radiative effect of airborne microplastics informed by new data. We perform sensitivity simulations with the same models used by R21 to identify the variables to which microplastic ERF is most sensitive, varying four factors that are key to determining the MP radiative effect: (1) MP colour, aided by new optical property data for coloured plastic polymers (as coloured microplastics are ubiquitous in the atmosphere[5,20,21]); (2) the MP size distribution, following literature analysis by Leusch et al.[22]; (3) the vertical extent of MP occurrence, informed by atmospheric transport studies[23–25]; and (4) the horizontal distribution of surface MP concentration, using new MP emissions data[3]. The simulations and models used are described in more detail in Methods.

Results

To isolate the impact of each of the aforementioned parameters on the MP direct radiative effect, we perform seven global circulation model simulations: a reference simulation replicating the result of R21, five one-at-a-time tests with different parameter values and a final 'Updated estimate' simulation that combines the parameter settings of the individual tests. Table 1 shows the scaled ERFs and instantaneous radiative forcings (IRFs, which unlike ERFs do not include the radiative impact of rapid adjustments; see section 'Modelling of radiative effects') for each simulation; the simulation parameters are given in Table 2 and described in section 'Microplastic morphotype and size distribution, Microplastic refractive index and Spatio-temporal distribution of microplastics'.

Our net ERFs span a range from −3.28 to +46.7 mW m^{-2}, with the bulk of this spread due to differences between the parameter settings of simulations rather than the uncertainty of individual simulations. Our uncertainties are determined only by interannual variability in the circulation model—each simulation is run with a prescribed spatial distribution

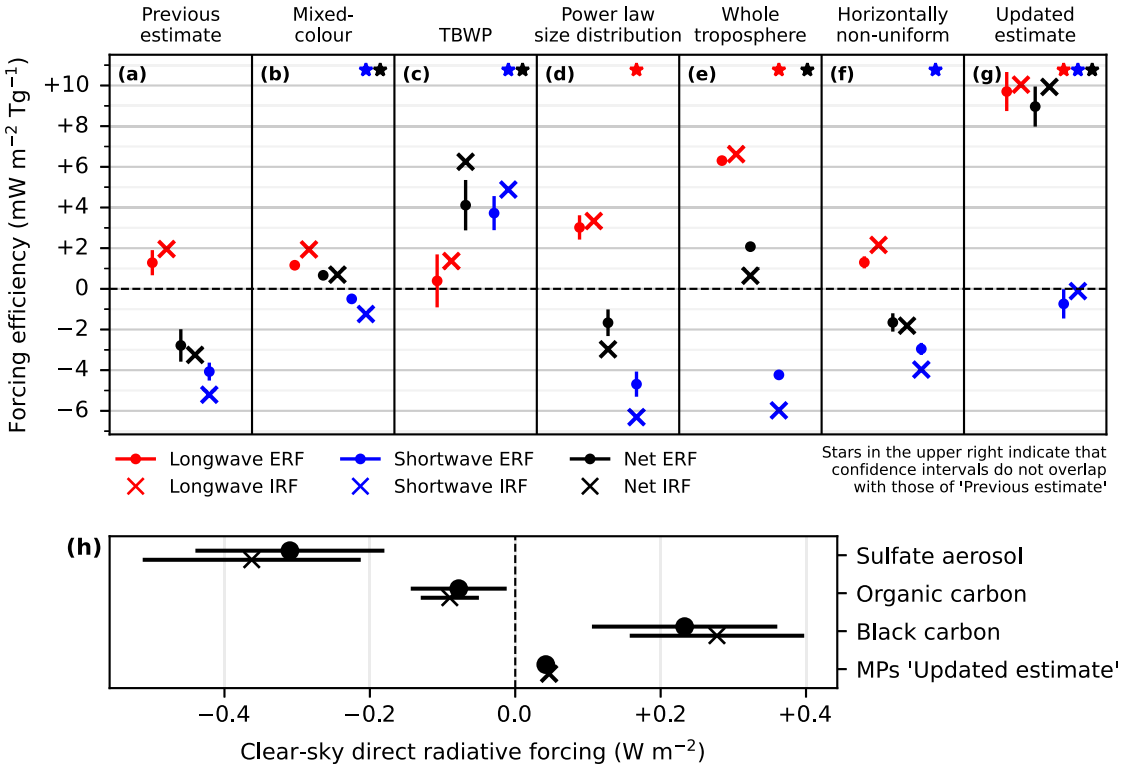

Fig. 1 | Radiative forcing of airborne microplastics. a–g Radiative forcing efficiency of microplastics (radiative forcing [mW m^{-2}] per unit total mass burden of MPs [Tg]) for each of our simulations (see Table 2 for details on simulation parameters). Red and blue symbols indicate the longwave and shortwave components of the forcing respectively; black symbols indicate the net forcing. Crosses indicate IRF efficiencies. Dots indicate ERF efficiencies, with bars indicating the 5–95% confidence interval of the 20 simulation years. Red, blue and black stars in the upper right of each subplot indicate, for that simulation, that the confidence interval of the corresponding ERF component (longwave, shortwave, or net respectively) does not overlap with that of the `Previous estimate' simulation (i.e. it is distinct in a statistically significant sense); note that simulations shown in (**b–f**) are one-at-a-time tests relative to `Previous estimate'. **h** Comparison of current best-estimate aerosol clear-sky net radiative forcing (ERF_{ari} and IRF_{ari}) and 'Updated estimate' MP radiative forcing calculated in this study. Note that IRF estimates have error bars only for non-MP species. ERF_{ari} for non-MP species was calculated as the sum of IRF_{ari} and non-cloud rapid adjustments provided by Thornhill et al.[56]; uncertainty estimates are displayed here as half the inter-model range over the four models for which the relevant data were available.

Fig. 2 | Size distributions of microplastic fragments used in sensitivity studies. a Gamma and **b** power law MP size distributions considered in this work. Both distributions are defined over 0.5 to 50 μm radius and are normalised to have the same total particle number concentration within the range 25–50 μm radius. Vertical tick marks and text indicate the average particle radius (r_1) and the effective radii of the area- and volume-average particles (r_2 and r_3, respectively) for the two distributions.

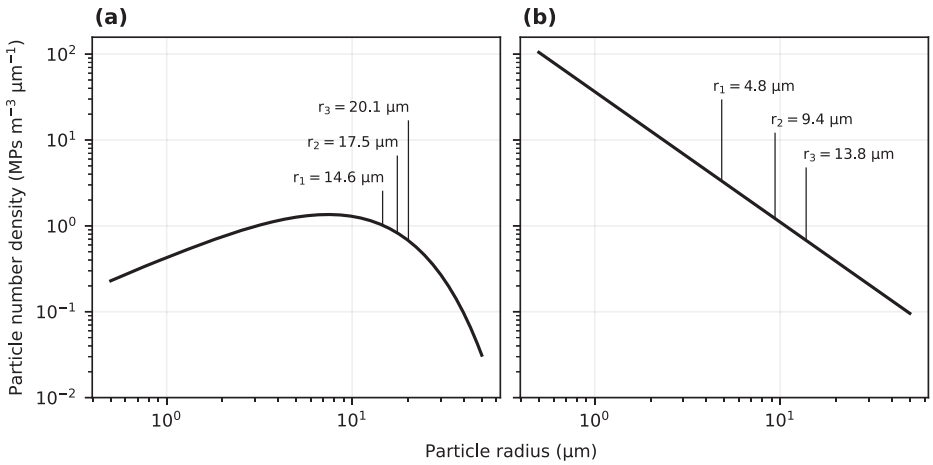

and optical properties, hence do not provide an estimate of parameter uncertainty. Our confidence intervals thus verify a statistically significant difference between parameter settings and demonstrate how radiative forcing is impacted by variations in that parameter.

Our net IRFs are generally only slightly greater in magnitude than the corresponding net ERFs, with a difference <3 mW m^{-2} indicative of rapid adjustments having a weak moderating influence on the radiative forcing.

Figure 1 shows the radiative forcing efficiency for each simulation, i.e. the radiative forcing per unit total MP mass burden. Our forcing efficiencies are relatively small, all <10 mW m^{-2} Tg^{-1} in magnitude, compared to e.g. −363 ± 139 mW m^{-2} Tg^{-1} for sulphate aerosol[26]. This is likely due to the larger average size of MPs in our simulations, around 5–20 μm in diameter (Fig. 2), compared to fine-mode sulphate aerosol at around 0.1 μm[27–29]. Smaller particles produce a stronger forcing efficiency due to their greater

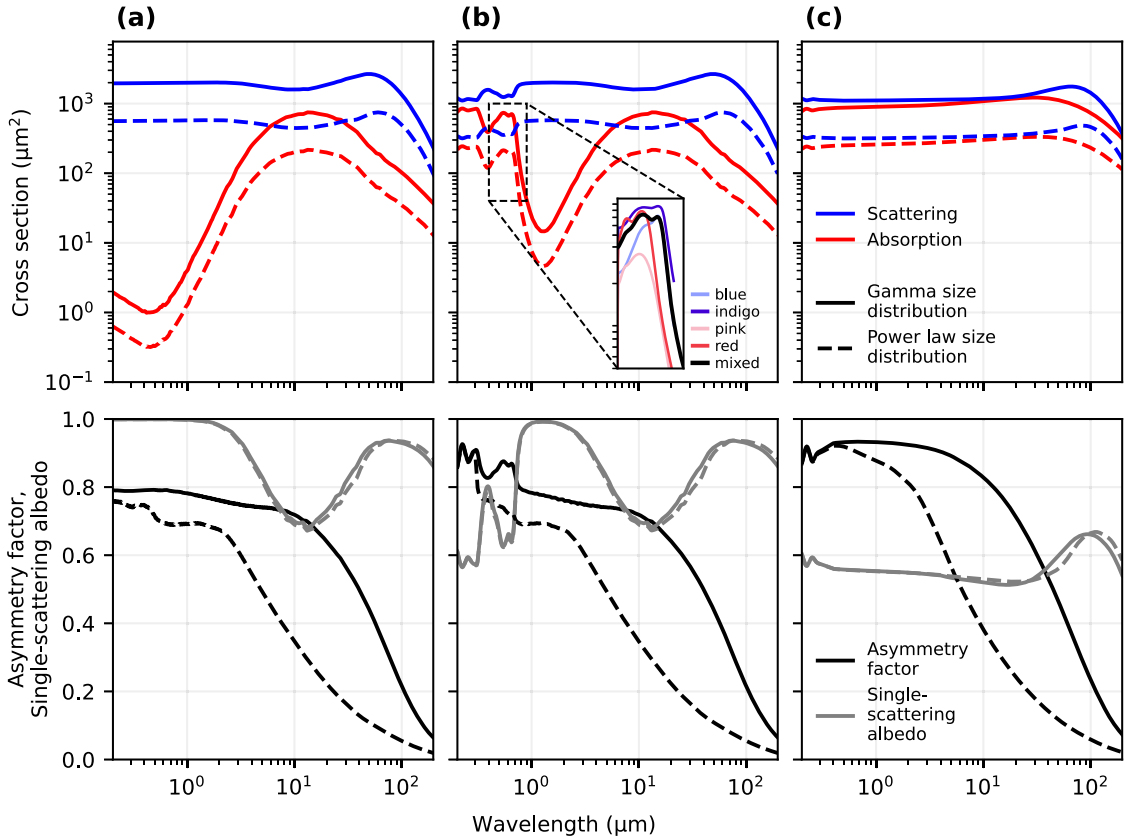

Fig. 3 | Optical properties of colourless and coloured microplastics. Absorption and scattering cross sections (top row) and asymmetry factor and single-scattering albedo (bottom row) for microplastic spheres of varying composition: **a** colourless plastic, **b** UV-absorbing mixed-colour plastic, **c** UV-absorbing colourless plastic mixed with 20% black carbon by weight. Solid lines indicate properties for particles following a gamma size distribution; dashed lines follow a power law size distribution. The inset plot (**b**) shows the absorption spectra of the four constituent colours that make up the mixed-colour plastic, following the gamma size distribution.

number concentration for the same total mass (see section 'Effect of size distribution on MP radiative forcing'), and the Mie scattering efficiency is greatest for particles with a comparable size to the wavelength (0.2–10 μm in the shortwave spectrum).

With the 'Previous estimate' simulation we repeat the result of R21 for microplastics confined to the boundary layer. We note that their simulation used a 1:1 mixture of fibres and fragments, whereas our simulations include only MP fragments (see Microplastic morphotype and size distribution). Scaling our ERF result (Table 1) to match their surface MP concentration (1 MP m^{-3}), we compute a radiative forcing of -0.094 ± 0.023 mW m^{-2} compared to their value of -0.746 ± 0.553 mW m^{-2}. Our result is smaller in magnitude and the confidence intervals do not quite overlap, though the discrepancy between the edges of the confidence intervals is small (-0.073 mW m^{-2}) and likely due to the absence of MP fibres in our simulations, which R21 demonstrated produce a stronger radiative forcing than fragments.

Effect of colour on MP radiative forcing

The effects of varying MP colour are shown in Fig. 1b–c (simulations 'Mixed-colour' and 'TBWP'), i.e. the calculated radiative forcing for MPs consisting of UV-absorbing mixed-colour plastic, and of UV-absorbing colourless plastic mixed with 20% black carbon (BC) by weight respectively.

The 'Mixed-colour' simulation (Fig. 1b) shows a shortwave cooling effect only 24% as large as that of the 'Previous estimate' simulation, owing to the warming effect of the absorption of solar radiation, due to the greater absorption cross-section of coloured plastic in the shortwave spectrum (Fig. 3). The shortwave effect is reduced enough that the net ERF efficiency is positive ($+0.67 \pm 0.17$ mW m^{-2} Tg^{-1}), indicating a net warming effect. The net ERF efficiency is, however, much smaller in magnitude than the 'Previous estimate' experiment as the short- and longwave components are close to compensating each other.

Studies have demonstrated a wide variety of colours presented by airborne MPs (e.g. reviews by Mbachu et al.[20], Shao et al.[21]), and the UV-absorption we model here is a measured property of the plastic polymer itself (see section 'Microplastic refractive index'), hence our mixed-colour optical properties are more representative of typical plastic. In measurements of coloured MPs, Liu et al.[19] also found an increase in the shortwave absorption cross-section due to pigmentation. Environmental aging and the diversity of both colourant and non-colourant additives used in plastic production[30] may introduce further variation in the full-spectrum scattering and absorption properties of plastic particles, highlighting the need for studies characterising the spectral properties of MPs in the environment. Until such studies are available, we consider the optical properties used in the 'Mixed-colour' simulation to best represent reality and recommend them for use in future radiative transfer modelling of airborne MPs.

The 'TBWP' simulation (Fig. 1c) clearly shows the impact of the increased absorption cross-section of BC-containing plastic (Fig. 3). The shortwave forcing efficiency has a similar magnitude to that of the 'Previous estimate' but is instead positive, resulting in a positive net forcing (i.e. net warming). This change in the net forcing is attributable solely to the absorption of shortwave radiation, as the longwave forcing efficiency is not significantly different from that of the 'Previous estimate' experiment. The net ERF efficiency of this simulation is small ($+4.12 \pm 1.24$ mW m^{-2} Tg^{-1}) compared to that of black carbon from fossil fuel and biofuel burning ($+2819 \pm 1235$ mW m^{-2} Tg^{-1}) but of the same order of magnitude as that of organic carbon and black carbon from biomass burning ($+14 \pm 310$ mW m^{-2} Tg^{-1})[26].

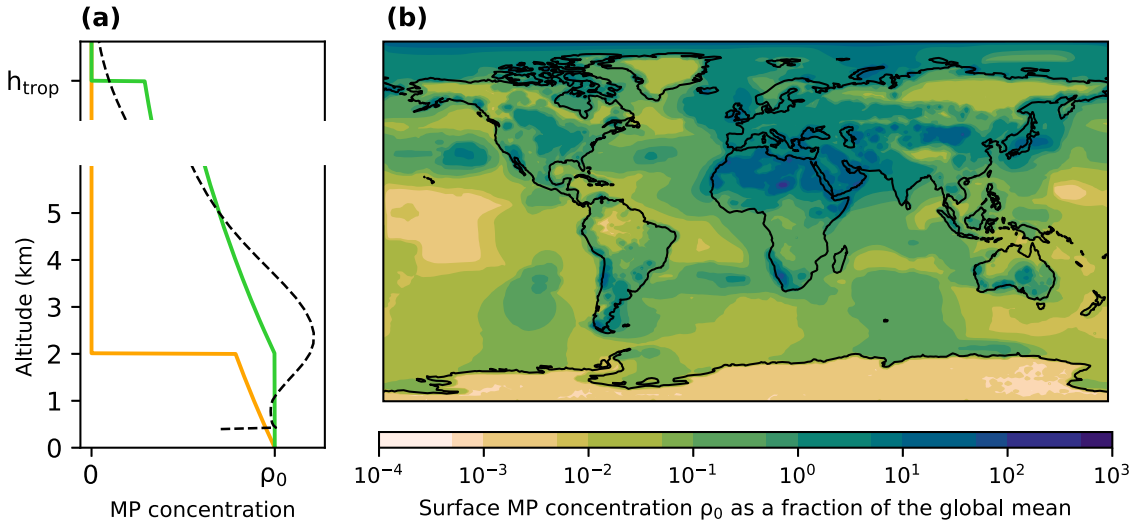

Fig. 4 | Vertical and horizontal spatial distributions of airborne microplastics. **a** Microplastic vertical distribution functions 'confined to <2 km' (orange line, Eq. (10)) and 'whole troposphere' (green line, Eq. (11)). Dashed line shows the distribution of MP fragments >1 μm in diameter in McErlich et al.[25]. **b** Surface microplastic concentration given by the non-uniform distribution, as a fraction of the global-average surface concentration. Map data from Natural Earth (www.naturalearthdata.com) and plotted using Cartopy[81].

Plastic particles mixed with black carbon are known to be present in the atmosphere as tire and brake-wear particles (TBWP) and may undergo atmospheric transport over significant distances[3,31]. We also see higher forcing efficiencies over land areas with a higher surface albedo (Fig. S1) where emissions inventories indicate the greatest emissions of TBWP from road traffic are found[3]. The discovery of black rubber particles in snow and the significant mass that TBWP may contribute relative to the mass of black carbon emissions suggests that TBWP in addition to black carbon may play a substantial role in snow albedo changes and the consequent acceleration of snow and ice melt[14,32–34]. The distinct warming properties of TBWP seen here compared to other MP particles (represented by the 'Previous estimate' experiment) therefore highlights the important role they may play in the overall MP radiative forcing.

Effect of size distribution on MP radiative forcing

The impact of a power law size distribution on the MP radiative forcing efficiency is shown in Fig. 1d (simulation 'Power law size distribution'). The longwave ERF efficiency for this experiment (3.02 ± 0.60 mW m^{-2} Tg^{-1}) is 2.3 × greater than that of the 'Previous estimate', likely due to the higher concentration of larger particles, with the power law size distribution resulting in more particles at radii >35 μm than the gamma size distribution (Fig. 2). These larger particles interact more strongly with longwave radiation; this can be seen in the smaller reduction in scattering cross sections at the long wavelength end of the spectrum compared to the spectra of gamma size distributed particles (Fig. 3).

In a literature analysis by Leusch et al.[22], a power law size distribution was found to be a good fit to MP size distributions across a range of environmental compartments, and a power law distribution is expected on theoretical grounds due to the fractal nature of particle fragmentation[35,36].

We set the lower bound of our size distributions at 1 μm diameter as this is close to the smallest particle size at which current analytical techniques can reliably measure particle number concentrations[37]. Smaller plastic particles, i.e. nanoplastics, are known to exist in the environment and their mass concentrations are beginning to be characterised (e.g. Materić et al.[38]). Nanoplastics may remain suspended in the atmosphere for longer, undergo greater horizontal and vertical transport and are more numerous at the same mass concentrations, amplifying their forcing efficiencies (Fig. S2). A recent study showed that the IRF of airborne nanoplastics could be several times larger than the corresponding IRF for microplastics[19]. However, analytical methods for quantifying nanoplastics are still under development. In particular, the nanoplastic size distributions used to inform Liu et al.[19]'s calculations were measured by pyrolysis-gas chromatography/mass spectrometry (py-GC/MS), which frequently identifies false positives, leading to measured nanoplastic concentrations 10 × higher than the thermal desorption-proton transfer reaction-mass spectrometry (TD-PTR-MS) method[39]. Future research should revisit nanoplastic radiative forcing once reliable global estimates of nanoplastic abundances and size distributions are available.

Effect of vertical distribution on MP radiative forcing

The effect of distributing MPs vertically throughout the whole troposphere is shown in Fig. 1e (simulation 'Whole troposphere'). The net ERF efficiency of this simulation (+2.07 ± 0.06 mW m^{-2} Tg^{-1}) is positive due to a substantial (5×) increase in the longwave forcing efficiency (+6.31 ± 0.06 mW m^{-2} Tg^{-1}) relative to that of the 'Previous estimate' (+1.29 ± 0.62 mW m^{-2} Tg^{-1}).

R21 also found a stronger radiative forcing when including MPs up to 10 km altitude than when confined to the lowest 2 km. Our 'whole troposphere' vertical distribution (see section 'Spatio-temporal distribution of microplastics') extends to the tropopause, up to 17 km altitude near the equator. Samset and Myhre[40] show that the black carbon forcing efficiency increases with altitude, such that a large proportion of the total BC forcing is contributed by BC at high altitude. We replicate this result in Fig. S3, which shows that the efficiency of longwave forcing increases with altitude such that a strong warming effect is contributed by high-altitude MPs. This suggests that the increase in longwave efficiency of our 'Whole troposphere' simulation is governed largely by the increase in the maximum altitude at which MPs occur.

Measurements and model studies of the vertical distribution of aerosols show that, subject to variations due to local conditions, aerosols are generally present above the boundary layer with concentrations decaying exponentially with height[41–44]. Transport modelling studies for airborne MPs have shown that MPs can be mixed throughout the troposphere, and may be transported into the stratosphere in limited amounts[23–25] (see also Fig. 4a). Tatsii et al.[23] show that particle shape can have a significant influence on the distance and altitude to which microplastics can be transported, with fibre morphotypes being dispersed further and higher due to their lower settling velocities. These findings suggest that our whole-troposphere vertical distribution provides a better approximation to the vertical extent of MPs than the 'Previous estimate' experiment, which has no MPs above 2 km altitude.

Regional and seasonal variations in the vertical profiles of aerosols are substantial and warrant addressing in the context of airborne MPs in future work, once more observational information on MP spatial distributions is available.

Effect of horizontal distribution on MP radiative forcing

The effect of a non-uniform MP surface concentration is shown in Fig. 1f. This simulation ('Horizontally non-uniform') produces a shortwave ERF efficiency 27% smaller in magnitude than that of the 'Previous estimate' simulation. This reduced shortwave cooling is due to the reduction in MP concentration over the open ocean, where surface albedo is low and scattering aerosols like (non BC-containing) MPs have a stronger cooling effect. Fig. S1d shows the difference in the distribution of total MP burden across surfaces of varying albedo. Surfaces with an albedo <0.08, over which colourless MPs have the strongest cooling effect, account for all ice-free ocean and underlie 62% of the total MP burden in the 'Previous estimate' simulation but only 18% in the 'Horizontally non-uniform' simulation.

Major airborne MP sources—synthetic textiles, tire and brake wear, industrial activity, landfill, waste incineration and degradation of macroplastics in the environment—are primarily terrestrial[1,21,45]. Macroplastics degrade to produce microplastics in the marine environment[46,47] and marine MPs can be emitted into the atmosphere[48–50], however MP number concentrations over the ocean are low[5,51] and the ocean is likely not a significant source of airborne MPs compared to the land surface[52–55]. This suggests that, even though the precise horizontal distribution of MP concentrations is poorly constrained by the observational evidence, the qualitative impact of the land–ocean contrast on the MP radiative effect that we find in our simulations is accurate.

Updated estimate of MP radiative forcing

The 'Updated estimate' simulation is shown in Fig. 1g, i.e. the combined effect of assuming mixed-colour plastic, a power law size distribution, a whole-troposphere vertical distribution and a non-uniform horizontal distribution. As discussed in the preceding sections, the parameter choices of this simulation provide a more realistic approximation of the real-world properties and distribution of airborne MPs than those of the 'Previous estimate'. This result therefore offers the most reliable estimate of the MP direct radiative forcing currently available in the literature, but excludes nanoplastic and TBWP radiative forcing as comparatively little is known about airborne nanoplastics and TBWPs have a very distinct spectral absorption cross-section.

The impact of each individual parameter choice can be seen in the 'Updated estimate' simulation. The shortwave forcing efficiency is reduced to near-zero (-0.74 ± 0.72 mW m^{-2} Tg^{-1}), as seen in simulations 'Mixed-colour', due to absorption in the shortwave spectrum, and 'Horizontally non-uniform', where reduction in MP concentrations over the oceans weakens the shortwave cooling effect. The longwave forcing efficiency ($+9.70 \pm 0.96$ mW m^{-2} Tg^{-1}) is considerably greater than the 'Previous estimate' simulation, as seen in simulations 'Power law size distribution', due to the relative increase in the concentration of larger particles, and 'Whole troposphere', due to the greater vertical extent of MPs. The combination of a weakened shortwave cooling and an amplified longwave warming results in the net ERF efficiency of this simulation being the most positive (warming) of any of our simulations ($+8.97 \pm 0.99$ mW m^{-2} Tg^{-1}). This is in contrast to the net negative (cooling) effect of the 'Previous estimate' simulation, and the cooling effects found by Revell et al.[16] and Pang et al.[18]. Liu et al.[19] also found a net warming due to MPs, however their work neglected the longwave effect, which we demonstrate is a large component of the overall MP ERF.

Considering comparable measures of radiative forcing for other aerosol species (i.e. clear-sky net ERFs and IRFs reported by Thornhill et al.[56]), shown in Fig. 1h, our new estimate of the MP radiative effect is small in comparison to that of other aerosol species, being e.g. 17% the magnitude of the black carbon ERF. Additionally, uncertainties in the aerosol radiative forcing arising from differences between models are large (even in absence of cloud-aerosol interactions, which introduce further uncertainty) and are not represented in our estimates which are produced with a single set of related models.

Discussion

In this work we investigate a range of variations on the optical properties and spatial distribution of airborne MPs, isolating the impact of these parameter variations on direct radiative forcing. Our sensitivity simulations yield an ERF ranging from -3.28 to $+46.7$ mW m^{-2}, and an ERF efficiency ranging from -3.58 to $+9.95$ mW m^{-2} Tg^{-1}, showing how these parameters can substantially impact the calculated radiative forcing.

At present, the paucity of quantitative constraints on parameter values preclude a true estimate of parameter uncertainty, however our results give what we suggest is a viable range for the microplastic ERF (-3.28 to $+46.7$ mW m^{-2}) and what we consider to be a most probable subset of that range ($+42.0 \pm 4.62$ mW m^{-2}, given by our 'Updated estimate'). We also emphasise the parameters which produce the greatest breadth in this viable range—the absorption cross-section in the shortwave spectrum, and the maximum altitude at which MPs are found—as areas on which future research should be focused.

The 'Updated estimate' simulation provides, to our knowledge, the most accurate assessment of the direct radiative forcing of airborne microplastics to date. Combining various lines of evidence to inform the most likely settings for each of the parameters considered, we obtain a radiative forcing efficiency of $+8.97 \pm 0.99$ mW m^{-2} Tg^{-1} (yielding a net ERF of $+42.0 \pm 4.62$ mW m^{-2} at an atmospheric plastic burden of 4.69 Tg). In contrast to the negative radiative forcing found by Revell et al.[16], Pang et al.[18], and in agreement with Liu et al.[19], this indicates that airborne MPs contribute overall to atmospheric warming via their direct radiative effect. This effect may be amplified by the presence of fibre MP morphologies in the real atmosphere, which produce a stronger radiative effect than the fragments we consider[16]. TBWP additionally form a substantial portion of the real atmospheric MP burden, over 50% in some countries[57] and contribute a warming effect in our 'TBWP' simulation which is not included in our 'Updated estimate'.

Evangelou et al.[55] recently identified that most microplastics inventories overestimate emissions. The non-uniform surface concentration of airborne MPs assumed in this study is lower in the global-mean than that reported by Evangelou et al.[55] (3.99 cf. their 31 MP m^{-3}), but higher in the median (0.34 cf. their 0.03 MP m^{-3}). Taking into account the different particle size ranges used (1–100 μm cf. their 5–100 μm) and scaling our 'Updated estimate' experiment to a median surface MP concentration matching that of their compiled observations yields an ERF of $+9.74$ mW m^{-2}. Either way, the range from this to our 'Updated estimate' ERF ($+42.0$ mW m^{-2}) would place microplastics above most of the anthropogenic forcers assessed by the Intergovernmental Panel on Climate Change (IPCC), of which around half have ERFs of 1 mW m^{-2} in magnitude or smaller[58].

MPs do not undergo rapid permanent removal from circulation in the total environment by any natural process, and may have extremely long residence times in numerous environmental compartments[6]. However, estimating future climate forcing is difficult due to multiple large uncertainties. Stegmann et al.[59] model annual plastic waste production under a moderate future greenhouse gas emissions scenario, projecting a total waste plastic mass 10.1 × greater than in 2023 by 2100. As a rough approximation, extrapolating our 'Updated estimate' to a 10.1 × greater surface concentration yields a radiative forcing of $+425 \pm 47$ mW m^{-2}. We acknowledge the very large uncertainties in plastic waste projections, rates of plastic degradation to produce microplastics and the airborne fraction of the global microplastic burden (e.g. the role of the ocean as a sink or reservoir for microplastics[2]). Nonetheless, a direct radiative forcing of $\sim+0.43$ W m^{-2} would be significant—larger than other aerosol species currently assessed by the IPCC (Fig. 1h).

Overall, we have illustrated the crucial role that uncertainties in microplastic optical properties, spatial distribution and total abundance play

in ERF estimates, highlighting the essential role of improved observation of the characteristics of microplastics in the environment. It seems clear that microplastics are overdue to be included as forcings in future climate change assessments, justifying more widespread attention towards this forcing source from the climate research, and perhaps policy, community.

Methods

Modelling of radiative effects

The radiative effects of atmospheric species such as aerosols or trace gases are quantified through metrics such as the effective radiative forcing (ERF) and instantaneous radiative forcing (IRF), which comprise the change in TOA radiative balance due to the perturbing species and varying degrees of atmospheric adjustment[60 61]. IRF is evaluated without allowing the atmospheric column to change, so does not include the radiative effects of so-called rapid adjustments, whereas ERF allows properties of the atmospheric column such as the temperature and moisture to change in response to the forcing on short timescales. Rapid adjustments are not coupled to the change in global-average surface air temperature and so do not constitute climate feedbacks[62 63]. ERF can be determined from the relationship between radiative forcing and feedback:

$$\Delta N = \mathrm{ERF} - \lambda \Delta T \tag{1}$$

where ΔN, λ and ΔT represent the TOA energy imbalance (W m^{-2}), the climate feedback parameter (W m^{-2} K^{-1}), and the change in global surface air temperature (K), respectively.

Here we present estimates only of the ERF due to aerosol-radiation interactions ($\mathrm{ERF_{ari}}$, henceforth simply ERF). MPs may have impacts on cloud formation[10–13 64] and hence a component of their ERF may be due to aerosol-cloud interactions (i.e. $\mathrm{ERF_{aci}}$). However, the model version used for this study is not configured to represent microplastic-cloud interactions and we focus only on direct radiative effects.

Estimates of the MP ERF were calculated from simulations using the Hadley Centre Global Environment Model version 3–Global Atmosphere model 7.1 (HadGEM3-GA7.1), developed by the UK Met Office and Momentum Partnership[65]. The model uses a regular 1.25° × 1.875° latitude-longitude grid with 85 unevenly-spaced vertical levels between the surface and 85 km altitude. The model radiative transfer scheme uses the Suite of Community Radiative Transfer codes based on Edwards and Slingo (SOCRATES; Edwards and Slingo[66]). As configured in HadGEM3-GA7.1, the shortwave part of the spectrum between 200 nm and 10 μm is divided into six spectral bands and the longwave part between 3.3 μm and 1 cm into nine spectral bands. Sea surface temperatures (SSTs) and sea-ice concentrations were prescribed from the Hadley Centre Global Sea Ice and SST observational dataset[67]. Greenhouse gas concentrations and aerosol emissions follow CMIP6 recommendations[68]. Each experiment was run for 21 years, from Sep 1988 to Sep 2009 and the first year of simulation was discarded as spin-up.

Following R21, we introduce airborne MPs in HadGEM3-GA7.1 using the non-interactive aerosol scheme (EasyAerosol), which enables the prescription of user-defined spatial distributions of aerosol species within the model. These aerosols interact only with radiation and are provided to the model as absorption and scattering coefficients on model grid cells and levels, hence they do not undergo interactive transport, emission or deposition, or microphysical processing. This configuration avoids making additional assumptions about microplastic properties such as settling velocities, scavenging coefficients, emission and resuspension rates, etc. MP optical properties were averaged across the model spectral bands, weighted in the shortwave by the incoming solar spectrum[69], and multiplied by the prescribed MP number concentration to convert to volume absorption and scattering coefficients.

ERFs are calculated as the change in the global-mean TOA clear-sky outgoing radiation relative to a control simulation which was run with no microplastics[61]. As SSTs in both simulations are prescribed, the surface air temperature response is suppressed and the change in TOA radiative balance approximates the ERF (equivalent to setting $\Delta T = 0$ in Eq. (1)). ERF is calculated separately for the shortwave and longwave components:

$$\mathrm{ERF_{SW}} = \uparrow \mathrm{SW_{Perturbed}} - \uparrow \mathrm{SW_{Control}} \tag{2}$$

$$\mathrm{ERF_{LW}} = \uparrow \mathrm{LW_{Perturbed}} - \uparrow \mathrm{LW_{Control}} \tag{3}$$

$$\mathrm{ERF_{Net}} = \mathrm{ERF_{SW}} + \mathrm{ERF_{LW}} \tag{4}$$

where ↑ denotes the global-mean TOA clear-sky outgoing radiation flux.

TOA radiative fluxes were calculated as global annual means of the daily mean time series. We assume each 20-year time series of ERF estimates $\boldsymbol{X}$ is t-distributed with $N - 1 = 19$ degrees of freedom, mean $\overline{\boldsymbol{X}}$, and scale $\sqrt{\mathrm{Var}[\boldsymbol{X}]/N}$ where $\mathrm{Var}[\boldsymbol{X}]$ denotes the variance of $\boldsymbol{X}$. The 5% to 95% confidence interval for the mean ERF was calculated from this t-distribution.

To estimate IRF, we employ the radiative transfer model SOCRATES which calculates radiative fluxes for a given atmospheric structure. Unlike HadGEM3-GA7.1, SOCRATES simulates no dynamics or physics processes, hence the atmosphere is held constant and no rapid adjustments can occur. For each latitude and longitude of the global HadGEM3-GA7.1 grid, we use annual-mean profiles of air temperature, moisture, ozone, and surface shortwave albedo calculated from ERA5 reanalyses[70]. Surface longwave emissivity was set to a constant value of 1. Fluxes were estimated using the two-stream approximation with a latitudinally-varying annual-mean daytime solar zenith angle. As the atmosphere is held constant for IRF calculations, no time series of annual IRFs are available from which to derive a confidence interval. As such we report only the global-mean IRF with no uncertainty.

We consider seven different experiments, detailed in Table 2, consisting of different combinations of optical properties (see section 'Microplastic morphotype and size distribution' and 'Microplastic refractive index') and prescribed spatio-temporal distribution (see section 'Spatio-temporal distribution of microplastics'). As in R21, we exaggerate the global-average surface MP concentration of each experiment in order to achieve a clear signal-to-noise ratio in the radiative forcing, and then scale the resultant IRF and ERF down to correspond to a realistic observationally-constrained global-average surface MP concentration, assuming that the MP radiative effect is proportional to the global-average surface MP concentration, i.e.

$$\mathrm{RF_{scaled}} = \mathrm{RF_{simulated}} \times \frac{[\mathrm{MP}]_{\mathrm{scaled}}}{[\mathrm{MP}]_{\mathrm{simulated}}} \tag{5}$$

where [MP] denotes the global-average surface MP concentration and $[\mathrm{MP}]_{\mathrm{scaled}} = 3.99$ MP m^{-3} between 50 and 100 μm diameter; note that we consider MPs ranging from 1 to 100 μm diameter, hence $[\mathrm{MP}]_{\mathrm{scaled}}$ is equivalent, over the full range of particle sizes, to a total number concentration of 27.3 MP m^{-3} and 91.7 MP m^{-3} for the gamma and power law size distributions respectively (see Microplastic morphotype and size distribution). Due to the different forcing efficiencies of each experiment, each required a different choice of $[\mathrm{MP}]_{\mathrm{simulated}}$ to achieve the same signal-to-noise ratio, hence for each experiment we prescribe a different global-average surface MP concentration (Table 2). Example calculations and further explanation of the scaling procedure are given in Supplementary Text S4.

This scaling procedure and Eq. (5) rely on the assumption of a proportional relationship between radiative forcing and the global-average surface concentration of MPs. We perform an additional two experiments, identical to 'Previous estimate' but with lower global-average surface MP concentrations, to demonstrate that proportionality holds over the range of surface concentrations and radiative forcings we consider (Fig. S4).

We report the radiative effect as both a global-average radiative forcing (mW m^{-2}; listed in Table 1) and as a forcing efficiency (mW m^{-2} Tg^{-1}; shown in Fig. 1). The forcing efficiency is defined as the global-average

radiative forcing per unit total mass burden of forcer. To calculate MP particle mass we assume a plastic density of 1.1 g cm^{-3}.

Microplastic morphotype and size distribution

MPs in the environment are classified according to their morphotype as fragments, fibres, or films. R21 considered fragments and fibres, neglecting films due to their lesser prevalence and a lack of information about their size distribution. Here, we assume that all MPs are in the form of fragments, neglecting fibres due to the complexity in calculating their optical properties, requiring additional assumptions about fibre size and shape, and because R21 already quantified the effect of morphotype on the MP radiative forcing. Their results for fragments and fibres found ERFs of −18.3 ± 62.5 and −38.8 ± 52.0 mW m^{-2}, respectively.

We assume fragments are approximately spherical, allowing for the calculation of their absorption and scattering cross sections and asymmetry factors using Mie theory, following the methodology of R21.

The distribution of the diameter of MP fragments in R21 was given by a gamma distribution with shape parameter 2 and scale parameter 15 μm determined by fitting to the limited observations available at that time (Eq. (6)). Following Leusch et al.[22] we also consider a power law size distribution (Eq. (7)).

$$\frac{\mathrm{d}N}{\mathrm{d}r} = A\left(\frac{2r}{15}\right)^2 \frac{1}{r} e^{-2r/15} \tag{6}$$

$$\frac{\mathrm{d}N}{\mathrm{d}r} = Br^{-\alpha} \tag{7}$$

where r is the particle radius in μm, $N(r)$ gives the number of particles in a bin of particle radius $(r, r + \mathrm{d}r)$, A and B (particles m^{-3} μm^{-1}) are normalisation constants that determine the total particle number concentration, and α determines the shape of the power law distribution. For both size distributions, we consider only MPs between 1 and 100 μm diameter (i.e. 0.5 μm ≤ r ≤ 50 μm, assuming a spherical shape).

Based on Leusch et al.[22], we set B = 36.6 MP m^{-3} μm^{-1} and α = 1.52 for outdoor airborne MPs. With these parameters, the power law predicts a MP number concentration of 3.99 MP m^{-3} in a bin of particle diameter from 50 to 100 μm (chosen as good observational data is available for such a size range). We match the gamma distribution to the number concentration in this range by choosing A = 27.6 MP m^{-3} μm^{-1} (i.e. such that $\int_{25\mu m}^{50\mu m} \frac{\mathrm{d}N}{\mathrm{d}r}\,\mathrm{d}r$ = 3.99 MP m^{-3} for both distributions). Over the full range of particle sizes (1 to 100 μm diameter) this is equivalent to a total number concentration of 27.3 MP m^{-3} and 91.7 MP m^{-3} for the gamma and power law size distributions, respectively. We use these particle number concentrations when scaling radiative forcings to realistic surface concentrations.

The two size distributions are shown in Fig. 2. Particle cross sections scale with the particle area, which is 3.5 × greater for the gamma size distribution than for the power law size distribution. Particle number concentrations scale inversely with the particle volume (when holding total mass constant), which is 3.1 × greater for the gamma size distribution than for the power law size distribution.

Microplastic refractive index

Only colourless MP particles were considered by R21, modelled by a polynomial fit to available measurements of the refractive indices of various plastic polymers. We present two alternatives to this: UV-absorbing mixed-colour plastic, accounting for observed absorption in the UV-visible spectrum that was neglected in R21; and BC-containing plastic, as an approximation to tire- and brake-wear particles (TBWP; Evangeliou et al.[3]). In both these cases, we account for the optical absorption using the complex refractive index, $m = n + ik$.

For colourless plastic (Fig. 3a) we use the refractive index of R21. For coloured plastics (Fig. 3b), we made laboratory measurements of the refractive index of coloured polyethylene terephthalate (PET) plastic films. In the UV spectrum (wavelengths 200–310 nm) we use the complex refractive index of PET reported by Ouchi[71]; in the UV-visible spectrum (wavelengths 360–800 nm) we use our measured refractive index; otherwise (wavelengths > 800 nm) we use the colourless plastic refractive index of R21. BC-containing plastic (Fig. 3c) was modelled as transparent plastic with black carbon spheres mixed homogeneously throughout[72], using the complex refractive index of PET reported by Ouchi[71] in the UV spectrum (wavelengths 200–310 nm) and the colourless plastic refractive index of R21 otherwise.

To measure the complex refractive index, we first measured the wavelength-dependent transmission $T(\lambda)$ of PET plastic films of thickness L ≈ 0.05 mm. Measurements were taken at wavelengths between 360 and 800 nm. The imaginary part k of the refractive index can then be deduced from Eq. (8).

$$k(\lambda) = \frac{2.303\lambda}{4\pi L}\left[-\log_{10} T(\lambda)\right] \tag{8}$$

To determine the effect of pigments on the real part n of the refractive index, the results were then fitted to Kramers-Kronig-consistent functions[73], in our case Lorentzian oscillators and then combined with the measured refractive index of a transparent polymer. Diffuse reflectance spectroscopy measurements were also performed to confirm that the results were consistent with reflection measurements and independent of scattering. A complete description of the measurement procedure is given by Glukhova[74]. The resultant refractive indices are shown in Fig. S5.

Measurements were made of one transparent PET film and four coloured PET films (blue, indigo, pink and red). The refractive index of the mixed-coloured plastic was modelled as an equal mixture of these four plastic colours. The peak in the imaginary part in the visible range corresponds to the dye absorption.

For each refractive index, we calculate the scattering and absorption spectra using Mie theory and average across the range of particle sizes weighted by the size distribution (see section 'Microplastic morphotype and size distribution'), viz.:

$$\overline{\sigma}(\lambda) = \frac{\int \sigma(r,\lambda)\,\mathrm{d}N}{\int \mathrm{d}N} = \frac{\int_{r_{\min}}^{r_{\max}} \sigma(r,\lambda)\frac{\mathrm{d}N}{\mathrm{d}r}\,\mathrm{d}r}{\int_{r_{\min}}^{r_{\max}} \frac{\mathrm{d}N}{\mathrm{d}r}\,\mathrm{d}r} \tag{9}$$

where $\sigma(r, \lambda)$ denotes the Mie scattering or absorption cross-section of a particle of radius r at wavelength λ, and $\overline{\sigma}(\lambda)$ denotes the size-average spectrum. Figure 3 shows the absorption and scattering spectra for each combination of refractive index and particle size distribution. Strong absorption peaks in the UV and visible spectrum are clearly seen in Fig. 3b–c due to the UV-absorption and presence of pigments. The addition of black carbon (Fig. 3d) results in a substantial increase in absorption across the whole spectrum. The power law size distribution gives smaller cross sections than the gamma size distribution due to the smaller average particle cross-sectional area. This affects scattering and absorption approximately equally, resulting in a largely unchanged single-scattering albedo. For both size distributions the asymmetry factor approaches zero as wavelength increases, reflecting the Rayleigh limit ($\lambda \gg r$), however the power law size distribution is closer to this limit at smaller wavelengths due to the smaller particle size, hence the asymmetry factor is smaller (i.e. more isotropic scattering) across much of the spectrum.

Spatio-temporal distribution of microplastics

We separate the spatio-temporal distribution of microplastics into a horizontally-varying surface concentration, denoted ρ_0, and a vertical distribution that describes how the MP concentration declines from the surface concentration in the vertical direction.

For the surface MP concentration ρ_0, R21 considered a constant value which we also use here and denote by 'uniform'. We additionally consider a spatially-varying ρ_0, derived from a particle transport simulation using FLEXPART and the MP emissions dataset of Evangeliou et al.[75], with

subsequent updates to ocean emissions to better account for the distribution of microplastics in surface waters per Isobe et al.[76]. The spatially-varying ρ_0 we consider here (denoted by 'non-uniform' and used in experiments 'Horizontally non-uniform' and 'Updated estimate') was taken from the time-average surface MP concentration of this simulation and is shown in Fig. 4b.

The vertical distribution of MPs in R21 was given by Eq. (10), which decreases the concentration of MPs approximately in accordance with the decrease in air density with increasing altitude. The MP concentration is set to zero above a cutoff altitude z_{cutoff}. R21 considered both $z_{\text{cutoff}} = 10$ km and $z_{\text{cutoff}} = 2$ km, approximating the tropopause and boundary layer height respectively. We consider this vertical distribution with $z_{\text{cutoff}} = 2$ km, as a more conservative base case for the 'Previous estimate' simulation and denote this distribution by 'confined to <2 km'.

$$\rho(z) = \rho_0 \times \begin{cases} 0.3^{z/10\text{km}} & z \le z_{\text{cutoff}} \\ 0 & z > z_{\text{cutoff}} \end{cases} \quad (10)$$

We consider an alternative vertical distribution (Eq. (11)) as a closer approximation to real-world conditions, particularly the impact of MP vertical transport. This distribution has a constant MP concentration from the surface up to an altitude z_{BL}, above which the MP concentration decreases like air density up to the tropopause. Above the tropopause the MP concentration is zero. We denote this distribution by 'whole troposphere'.

$$\rho(z) = \rho_0 \times \begin{cases} 1 & z \le z_{\text{BL}} \\ 0.3^{(z-z_{\text{BL}})/10\text{km}} & z_{\text{BL}} < z \le z_{\text{trop}} \\ 0 & z > z_{\text{trop}} \end{cases} \quad (11)$$

where z_{trop} is the monthly-mean tropopause height taken from the control HadGEM3-GA7.1 simulation. We set $z_{\text{BL}} = 2$ km as an approximation to the global-average depth of the planetary boundary layer (PBL). Both vertical distributions are shown in Fig. 4a.

This distribution is intended to approximate an average vertical distribution of aerosols in the real atmosphere (e.g. Xiang et al.[77], Sheridan et al.[78]) and is in good agreement with the global-average vertical distribution of MPs in the results of McErlich et al.[25] (shown in Fig. 4a). The assumption of a constant PBL height $z_{\text{BL}} = 2$ km (see section 'Spatio-temporal distribution of microplastics' and Eq. (11)) is not a good approximation to reality, where the PBL varies in depth between ~500 m and ~3 km depending on season, land surface and local atmospheric conditions[79,80]. However, variations in the value of z_{BL} only negligibly affect our IRF results (Fig. S3 and accompanying text).

Data availability

All data used in this study are available on GitHub at https://github.com/felix-goddard/microplastic-direct-radiative-effects.

Code availability

Code written for this study is available on GitHub at https://github.com/felix-goddard/microplastic-direct-radiative-effects.

Received: 23 June 2026; Accepted: 10 August 2026;
Published online: 10 September 2026

References

1. Zhao, X. et al. Airborne microplastics: occurrence, sources, fate, risks and mitigation. *Sci. Total Environ.* **858**, 159943, https://doi.org/10.1016/j.scitotenv.2022.159943 (2023).
2. Allen, D. et al. Microplastics and nanoplastics in the marine-atmosphere environment. *Nat. Rev. Earth Environ.* **3**, 393–405, https://doi.org/10.1038/s43017-022-00292-x (2022).
3. Evangeliou, N. et al. Atmospheric transport is a major pathway of microplastics to remote regions. *Nat. Commun.* **11**, 3381. https://doi.org/10.1038/s41467-020-17201-9 (2020).
4. Allen, S. et al. Atmospheric transport and deposition of microplastics in a remote mountain catchment. *Nat. Geosci.* **12**, 339–344, https://doi.org/10.1038/s41561-019-0335-5 (2019).
5. Chen, Q. et al. Long-range atmospheric transport of microplastics across the southern hemisphere. *Nat. Commun.* **14**, 7898. https://doi.org/10.1038/s41467-023-43695-0 (2023).
6. Sonke, J. E. et al. A mass budget and box model of global plastics cycling, degradation and dispersal in the land-ocean-atmosphere system. *Microplastics Nanoplastics* **2**, 28, https://doi.org/10.1186/s43591-022-00048-w (2022).
7. Xu, J.-L., Lin, X., Wang, J. J. & Gowen, A. A. A review of potential human health impacts of micro- and nanoplastics exposure. *Sci. Total Environ.* **851**, 158111, https://doi.org/10.1016/j.scitotenv.2022.158111 (2022).
8. Twomey, S. The influence of pollution on the shortwave Albedo of clouds. *J. Atmos. Sci.* **34**, 1149–1152 (1977).
9. Albrecht, B. A. Aerosols, cloud microphysics, and fractional cloudiness. *Science* **245**, 1227–1230, https://doi.org/10.1126/science.245.4923.1227 (1989).
10. Aeschlimann, M., Li, G., Kanji, Z. A. & Mitrano, D. M. Potential impacts of atmospheric microplastics and nanoplastics on cloud formation processes. *Nat. Geosci.* **15**, 967–975, https://doi.org/10.1038/s41561-022-01051-9 (2022).
11. Ganguly, M. & Ariya, P. A. Ice nucleation of model nanoplastics and microplastics: a novel synthetic protocol and the influence of particle capping at diverse atmospheric environments. *ACS Earth Space Chem.* **3**, 1729–1739, https://doi.org/10.1021/acsearthspacechem.9b00132 (2019).
12. Seifried, T. M. et al. Microplastic particles contain ice nucleation sites that can be deactivated by atmospheric aging. https://doi.org/10.26434/chemrxiv-2024-k0sgz (2024).
13. Tatsii, D., Gasparini, B., Evangelou, I., Bucci, S. & Stohl, A. Do microplastics contribute to the total number concentration of ice nucleating particles? *J. Geophys. Res. Atmos.* **130**, e2024JD042827 (2025).
14. Reynolds, R. L. et al. Microplastic and associated black particles from road-tire wear: implications for radiative effects across the cryosphere and in the atmosphere. *J. Geophys. Res. Atmos.* **129**, e2024JD041116, https://doi.org/10.1029/2024JD042827 (2024).
15. Ming, J. & Wang, F. *Microplastics' Hidden Contribution to Snow Melting*. https://eos.org/opinions/microplastics-hidden-contribution-to-snow-melting (2021).
16. Revell, L. E., Kuma, P., Le Ru, E. C., Somerville, W. R. C. & Gaw, S. Direct radiative effects of airborne microplastics. *Nature* **598**, 462–467, https://doi.org/10.1038/s41586-021-03864-x (2021).
17. Yang, H. et al. Influence of regional environmental variables on the radiative forcing of atmospheric microplastics. *Eco-Environ. Health* **4**, 100128, https://doi.org/10.1016/j.eehl.2024.11.002 (2025).
18. Pang, Q., Wang, X., Zhuang, B., Wang, H. & Zhang, Y. A model-based estimate for the direct radiative effect of atmospheric microplastics. *Atmos. Environ.* 121305. https://doi.org/10.1016/j.atmosenv.2025.121305 (2025).
19. Liu, Y. et al. Atmospheric warming contributions from airborne microplastics and nanoplastics. *Nat. Clim. Change* 1–8. https://doi.org/10.1038/s41558-026-02620-1 (2026).
20. Mbachu, O., Jenkins, G., Pratt, C. & Kaparaju, P. A new contaminant superhighway? A review of sources, measurement techniques and fate of atmospheric microplastics. *Water Air Soil Pollut.* **231**, 85, https://doi.org/10.1007/s11270-020-4459-4 (2020).
21. Shao, L. et al. Airborne microplastics: a review of current perspectives and environmental implications. *J. Clean. Prod.* **347**, 131048, https://doi.org/10.1016/j.jclepro.2022.131048 (2022).

22. Leusch, F. D., Lu, H.-C., Perera, K., Neale, P. A. & Ziajahromi, S. Analysis of the literature shows a remarkably consistent relationship between size and abundance of microplastics across different environmental matrices. *Environ. Pollut.* **319**, 120984, https://doi.org/10.1016/j.envpol.2022.120984 (2023).
23. Tatsii, D. et al. Shape matters: long-range transport of microplastic fibers in the atmosphere. *Environ. Sci. Technol.* **58**, 671–682, https://doi.org/10.1021/acs.est.3c08209 (2024).
24. Bucci, S., Richon, C. & Bakels, L. Exploring the transport path of oceanic microplastics in the atmosphere. *Environ. Sci. Technol.* **58**, 14338–14347, https://doi.org/10.1021/acs.est.4c03216 (2024).
25. McErlich, C. et al. Description and evaluation of airborne microplastics in the United Kingdom Earth System Model (UKESM1.1) using GLOMAP-mode. *Geosci. Model Dev.* **18**, 8827–8854, https://doi.org/10.5194/gmd-18-8827-2025 (2025).
26. Myhre, G. et al. Radiative forcing of the direct aerosol effect from AeroCom Phase II simulations. *Atmos. Chem. Phys.* **13**, 1853–1877, https://doi.org/10.5194/acp-13-1853-2013 (2013).
27. Liu, X., Penner, J. E. & Herzog, M. Global modeling of aerosol dynamics: model description, evaluation, and interactions between sulfate and nonsulfate aerosols. *J. Geophys. Res. Atmos.* **110**, 2004JD005674, https://doi.org/10.1029/2004JD005674 (2005).
28. Ma, X. & Von Salzen, K. Dynamics of the sulphate aerosol size distribution on a global scale. **111**, 2005JD006620. https://doi.org/10.1029/2005JD006620 (2006).
29. Mészáros, Á On the size distribution of atmospheric aerosol particles of different composition. *Atmos. Environ.* **11**, 1075–1081, https://doi.org/10.1016/0004-6981(77)90237-2 (1977).
30. Wiesinger, H., Wang, Z. & Hellweg, S. Deep dive into plastic monomers, additives, and processing aids. *Environ. Sci. Technol.* **55**, 9339–9351, https://doi.org/10.1021/acs.est.1c00976 (2021).
31. Grigoratos, T. & Martini, G. Brake wear particle emissions: a review. *Environ. Sci. Pollut. Res.* **22**, 2491–2504, https://doi.org/10.1007/s11356-014-3696-8 (2015).
32. Bergmann, M. et al. White and wonderful? Microplastics prevail in snow from the Alps to the Arctic. *Sci. Adv.* **5**, eaax1157, https://doi.org/10.1126/sciadv.aax1157 (2019).
33. Abbasi, S. et al. Microplastics captured by snowfall: a study in Northern Iran. *Sci. Total Environ.* **822**, 153451, https://doi.org/10.1016/j.scitotenv.2022.153451 (2022).
34. Kang, S., Zhang, Y., Qian, Y. & Wang, H. A review of black carbon in snow and ice and its impact on the cryosphere. *Earth Sci. Rev.* **210**, 103346, https://doi.org/10.1016/j.earscirev.2020.103346 (2020).
35. Kooi, M. & Koelmans, A. A. Simplifying microplastic via continuous probability distributions for size, shape, and density. *Environ. Sci. Technol. Lett.* **6**, 551–557, https://doi.org/10.1021/acs.estlett.9b00379 (2019).
36. Wang, L. et al. Modeling the conditional fragmentation-induced microplastic distribution. *Environ. Sci. Technol.* **55**, 6012–6021, https://doi.org/10.1021/acs.est.1c01042 (2021).
37. Chen, G., Fu, Z., Yang, H. & Wang, J. An overview of analytical methods for detecting microplastics in the atmosphere. *TrAC Trends Anal. Chem.* **130**, 115981, https://doi.org/10.1016/j.trac.2020.115981 (2020).
38. Materić, D. et al. Micro- and nanoplastics in alpine snow: a new method for chemical identification and (semi) quantification in the nanogram range. *Environ. Sci. Technol.* **54**, 2353–2359, https://doi.org/10.1021/acs.est.9b07540 (2020).
39. Aves, A. et al. Comparative assessment of five analytical methods for airborne microplastics highlights importance of identifying sub-10 µm methods. *Sci. Rep*. https://www.nature.com/articles/s41598-026-49405-2 (2026).
40. Samset, B. H. & Myhre, G. Vertical dependence of black carbon, sulphate and biomass burning aerosol radiative forcing. *Geophys. Res. Lett.* **38**, https://doi.org/10.1029/2011GL049697 (2011).
41. Satheesh, S. K., Vinoj, V. & Moorthy, K. K. Vertical distribution of aerosols over an urban continental site in India inferred using a micro pulse lidar. *Geophys. Res. Lett.* **33**, 2006GL027729, https://doi.org/10.1029/2006GL027729 (2006).
42. Koffi, B. et al. Application of the CALIOP layer product to evaluate the vertical distribution of aerosols estimated by global models: AeroCom phase I results. *J. Geophys. Res. Atmos.* **117**, 2011JD016858, https://doi.org/10.1029/2011JD016858 (2012).
43. Zhang, Q., Ma, X., Tie, X., Huang, M. & Zhao, C. Vertical distributions of aerosols under different weather conditions: analysis of in-situ aircraft measurements in Beijing, China. *Atmos. Environ.* **43**, 5526–5535, https://doi.org/10.1016/j.atmosenv.2009.05.037 (2009).
44. Sun, X. et al. Seasonal and vertical variations in aerosol distribution over Shijiazhuang, China. *Atmos. Environ.* **81**, 245–252, https://doi.org/10.1016/j.atmosenv.2013.08.009 (2013).
45. Sridharan, S., Kumar, M., Singh, L., Bolan, N. S. & Saha, M. Microplastics as an emerging source of particulate air pollution: a critical review. *J. Hazard. Mater.* **418**, 126245, https://doi.org/10.1016/j.jhazmat.2021.126245 (2021).
46. Gewert, B., M. Plassmann, M. & MacLeod, M. Pathways for degradation of plastic polymers floating in the marine environment. *Environ. Sci. Process. Impacts* **17**, 1513–1521, https://doi.org/10.1039/C5EM00207A (2015).
47. Chamas, A. et al. Degradation rates of plastics in the environment. *ACS Sustain. Chem. Eng.* **8**, 3494–3511, https://doi.org/10.1021/acssuschemeng.9b06635 (2020).
48. Allen, S. et al. Examination of the ocean as a source for atmospheric microplastics. *PLoS ONE* **15**, e0232746, https://doi.org/10.1371/journal.pone.0232746 (2020).
49. Harb, C., Pokhrel, N. & Foroutan, H. Quantification of the emission of atmospheric microplastics and nanoplastics via sea spray. *Environ. Sci. Technol. Lett.* **10**, 513–519, https://doi.org/10.1021/acs.estlett.3c00164 (2023).
50. Shaw, D. B., Li, Q., Nunes, J. K. & Deike, L. Ocean emission of microplastic. *PNAS Nexus* **2**, pgad296, https://doi.org/10.1093/pnasnexus/pgad296 (2023).
51. Wang, X. et al. Exponential decrease of airborne microplastics: from megacity to open ocean. *Sci. Total Environ.* **849**, 157702, https://doi.org/10.1016/j.scitotenv.2022.157702 (2022).
52. Yang, S., Lu, X. & Wang, X. A perspective on the controversy over global emission fluxes of microplastics from ocean into the atmosphere. *Environ. Sci. Technol.* **58**, 12304–12312, https://doi.org/10.1021/acs.est.4c03182 (2024).
53. Yang, S. et al. Constraining microplastic particle emission flux from the ocean. *Environ. Sci. Technol. Lett.* **9**, 513–519, https://doi.org/10.1021/acs.estlett.2c00214 (2022).
54. Yang, S., Brasseur, G., Walters, S., Lichtig, P. & Li, C. W. Y. Global atmospheric distribution of microplastics with evidence of low oceanic emissions. *npj Clim. Atmos. Sci.* **8**, 1–10, https://doi.org/10.1038/s41612-025-00914-3 (2025).
55. Evangelou, I., Bucci, S. & Stohl, A. Atmospheric microplastic emissions from land and ocean. *Nature* 1–4. https://doi.org/10.1038/s41586-025-09998-6 (2026).
56. Thornhill, G. D. et al. Effective radiative forcing from emissions of reactive gases and aerosols – a multi-model comparison. *Atmos. Chem. Phys.* **21**, 853–874, https://doi.org/10.5194/acp-21-853-2021 (2021).
57. Zhang, M. et al. A comprehensive review of tyre wear particles: formation, measurements, properties, and influencing factors. *Atmos. Environ.* **297**, 119597, https://doi.org/10.1016/j.atmosenv.2023.119597 (2023).
58. Dentener, F., Hall, B. & Smith, C. Annex III: Tables of historical and projected well-mixed greenhouse gas mixing ratios and effective radiative forcing of all climate forcers. In *Climate Change 2021: The*

Physical Science Basis (eds Masson-Delmotte, V. et al.) 2139–2152 (Cambridge University Press, 2021).
59. Stegmann, P., Daioglou, V., Londo, M., van Vuuren, D. P. & Junginger, M. Plastic futures and their CO2 emissions. *Nature* **612**, 272–276, https://doi.org/10.1038/s41586-022-05422-5 (2022).
60. Forster, P. et al. The Earth's energy budget, climate feedbacks, and climate sensitivity. In *Climate Change 2021: The Physical Science Basis. Contribution of Working Group I to the Sixth Assessment Report of the Intergovernmental Panel on Climate Change* (eds Masson-Delmotte, V. et al.) 923–1054 (Cambridge University Press, 2021).
61. Forster, P. M. et al. Recommendations for diagnosing effective radiative forcing from climate models for CMIP6. *J. Geophys. Res. Atmos.* **121**, 12,460–12,475 (2016).
62. Sherwood, S. C. et al. Adjustments in the forcing-feedback framework for understanding climate change. *Bull. Am. Meteorol. Soc.* **96**, 217–228, https://doi.org/10.1175/BAMS-D-13-00167.1 (2015).
63. Boucher, O. et al. Clouds and Aerosols. In *Climate Change 2013: The Physical Science Basis. Contribution of Working Group I to the Fifth Assessment Report of the Intergovernmental Panel on Climate Change* (eds Stocker, T. F. et al.) 571–657 (Cambridge University Press, 2013).
64. Wang, Y. et al. Airborne hydrophilic microplastics in cloud water at high altitudes and their role in cloud formation. *Environ. Chem. Lett.* **21**, 3055–3062, https://doi.org/10.1007/s10311-023-01626-x (2023).
65. Walters, D. et al. The Met Office Unified Model global atmosphere 7.0/7.1 and JULES global land 7.0 configurations. *Geosci. Model Dev.* **12**, 1909–1963 (2019).
66. Edwards, J. M. & Slingo, A. Studies with a flexible new radiation code. I: choosing a configuration for a large-scale model. *Q. J. R. Meteorol. Soc.* **122**, 689–719, https://doi.org/10.1002/qj.49712253107 (1996).
67. Titchner, H. A. & Rayner, N. A. The Met Office Hadley Centre sea ice and sea surface temperature data set, version 2: 1. Sea ice concentrations. *J. Geophys. Res. Atmos.* **119**, 2864–2889 (2014).
68. Lamarque, J.-F. et al. Historical (1850–2000) gridded anthropogenic and biomass burning emissions of reactive gases and aerosols: methodology and application. *Atmos. Chem. Phys.* **10**, 7017–7039 (2010).
69. Lean, J. L. & DeLand, M. T. How does the Sun's spectrum vary? *J. Clim*. **25**, 2555–2560 (2012).
70. Hersbach, H. et al. The ERA5 global reanalysis. *Q. J. R. Meteorol. Soc.* **146**, 1999–2049, https://doi.org/10.1002/qj.3803 (2020).
71. Ouchi, I. Anisotropic absorption and reflection spectra of poly (ethylene terephthalate) films in ultraviolet region. *Polym. J.* **15**, 225–243, https://doi.org/10.1295/polymj.15.225 (1983).
72. Markel, V. A. Introduction to the Maxwell Garnett approximation: tutorial. *J. Opt. Soc. Am. A* **33**, 1244, https://doi.org/10.1364/JOSAA.33.001244 (2016).
73. Djorović, A., Meyer, M., Darby, B. L. & Le Ru, E. C. Accurate modeling of the polarizability of dyes for electromagnetic calculations. *ACS Omega* **2**, 1804–1811, https://doi.org/10.1021/acsomega.7b00171 (2017).
74. Glukhova, S. *Optical Properties of Matter: From Plasmonic Nanoparticles to Airborne Microplastics*. Doctor of Philosophy, Te Herenga Waka—Victoria University of Wellington https://doi.org/10.26686/3480-kjsc (2026).
75. Evangeliou, N., Tichý, O., Eckhardt, S., Zwaaftink, C. G. & Brahney, J. Sources and fate of atmospheric microplastics revealed from inverse and dispersion modelling: From global emissions to deposition. *J. Hazard. Mater.* **432**, 128585, https://doi.org/10.1016/j.jhazmat.2022.128585 (2022).
76. Isobe, A. et al. A multilevel dataset of microplastic abundance in the world's upper ocean and the Laurentian Great Lakes. *Microplastics Nanoplastics* **1**, 16, https://doi.org/10.1186/s43591-021-00013-z (2021).
77. Xiang, Y. et al. Vertical profile of aerosols in the Himalayas revealed by lidar: new insights into their seasonal/diurnal patterns, sources, and transport. *Environ. Pollut.* **285**, 117686, https://doi.org/10.1016/j.envpol.2021.117686 (2021).
78. Sheridan, P. J., Andrews, E., Ogren, J. A., Tackett, J. L. & Winker, D. M. Vertical profiles of aerosol optical properties over central Illinois and comparison with surface and satellite measurements. *Atmos. Chem. Phys.* **12**, 11695–11721, https://doi.org/10.5194/acp-12-11695-2012 (2012).
79. McGrath-Spangler, E. L. & Denning, A. S. Global seasonal variations of midday planetary boundary layer depth from CALIPSO space-borne LIDAR. *J. Geophys. Res. Atmos.* **118**, 1226–1233, https://doi.org/10.1002/jgrd.50198 (2013).
80. Chan, K. M. & Wood, R. The seasonal cycle of planetary boundary layer depth determined using COSMIC radio occultation data. *J. Geophys. Res. Atmos.* **118**, 12,422–12,434, https://doi.org/10.1002/2013JD020147 (2013).
81. Met Office. Cartopy: a cartographic Python library with a matplotlib interface. Exeter, Devon (2010–2015). http://scitools.org.uk/cartopy.

Acknowledgements

This research was supported by the Royal Society Te Apārangi Marsden Fund (contracts 22-UOC-088 and VUW-2118) and Rutherford Discovery Fellowships (22-UOC-14), administered by the Royal Society Te Apārangi. N.E. was supported by the Norwegian Research Council (NFR) project MAGIC (Airborne Microplastic Detection, Origin, Transport and Global Radiative Impact, Project No.: 334086). We acknowledge the UK Met Office for the use of HadGEM3-GA7.1 and SOCRATES. The authors wish to acknowledge use of the eResearch Infrastructure Platform hosted by the Crown company, Research and Education Advanced Network New Zealand (REANNZ) Ltd., and funded by the Ministry of Business, Innovation & Employment: https://www.reannz.co.nz.

Author contributions

F.W.G. and L.E.R. designed the study and wrote the main text. F.W.G. performed the model simulations, with assistance from C.M., C.H. and D.F., using code developed by P.K., and emissions data provided by N.E. S.G. and E.C.L.R. measured plastic refractive indices. All authors contributed to the discussion and reviewed the manuscript. L.E.R. obtained funding for the study.

Competing interests

The authors declare no competing interests.

Additional information

Supplementary information The online version contains supplementary material available at https://doi.org/10.1038/s44454-026-00058-w.

Correspondence and requests for materials should be addressed to Felix W. Goddard or Laura E. Revell.